RESEARCH ARTICLE
PLANETARY SCIENCES

Earth and Planetary Physics
8: 686–702, 2024
doi: 10.26464/epp2024062

Mantle avalanches in a Venus-like stagnant lid planet

Madeleine C. Kerr*, and Dave R. Stegman

Institute of Geophysics and Planetary Physics, Scripps Institution of Oceanography, University of California, San Diego, La Jolla, CA, USA

Key Points:

- Venus adiabats (>1700 K) pass through the wadsleyite + majorite + ferropericlase mineral phase, characterized by negative thermal expansivity.
- In stagnant lid convection small cold Rayleigh–Taylor instabilities layer above and are deflected by this zone of reversed thermal buoyancy.
- In 1900 K stagnant lid models, layered drips coalesce into mantle avalanches, a possible convective regime for present-day Venus.

Citation: Kerr, M. C., and Stegman, D. R. (2024). Mantle avalanches in a Venus-like stagnant lid planet. *Earth Planet. Phys.*, *8*(5), 686–702. http://doi.org/10.26464/epp2024062

Abstract: Stagnant lid planets are characterized by a globe-encircling, conducting lid that is thick and strong, which leads to reduced global surface heat flows. Consequently, the mantles of such planets can have warmer interiors than Earth, and interestingly, a pyrolitic mantle composition under warmer conditions is predicted to have a distinctly different mantle transition zone compared to the present-day Earth (Hirose, 2002; Stixrude and Lithgow-Bertelloni, 2011; Ichikawa et al., 2014; Dannberg et al, 2022). Instead of olivine primarily transforming into its higher-pressure polymorphs such as wadsleyite and then ringwoodite, at pressures corresponding to 410 km and 520 km depth in Earth, respectively, it instead transforms into a mineral assemblage of wadsleyite, majorite, and ferropericlase (WMF), and then to majorite + ferropericlase (MF), before finally transforming into bridgmanite at pressures corresponding to 660 km depth in Earth (Stixrude and Lithgow-Bertelloni, 2011; Ichikawa et al., 2014). Convective motions in stagnant lid planets are dominated by small-scale instabilities (cold drips) forming within the mobile rheological sublayer under the rigid lid. Using ASPECT and a thermodynamic model of a pyrolitic mantle composition generated by HeFESTo, we show that under certain conditions, the small drips can pond atop the WMF-MF mineral phase transition. The barrier to convective flow arises from the WMF mineral phase assemblage having an effective negative thermal expansivity (Stixrude and Lithgow-Bertelloni, 2022). Although large-scale downwellings that typically occur within mobile lid planets are able to pass through the WMF zone without difficulty (Dannberg et al., 2022; Li RP et al., 2024), the smaller and less negatively buoyant nature of downwelling drips in stagnant lid planets are more susceptible to these effects, which leads to an ephemeral layering of the mantle. Our numerical models show that in stagnant lid planets with mantle potential temperatures that exceed 1900 K, the smaller, cold drips from the lid continue to pile up until enough of them have coalesced that they collectively avalanche as a larger instability into the deeper interior.

Keywords: Venus; mantle avalanches; numerical modelling; phase transitions

1. Introduction

Despite sharing many similarities, for example forming in close proximity to each other, having similar radii, and both having differentiated into a metallic core surrounded by a silicate mantle, Earth and Venus have a profoundly different expression of tectonism and volcanism on their surface. Plate tectonics on Earth provides a conceptual framework for understanding how the planet's outermost layer, the lithosphere, is broken into tectonic plates which are the surface manifestation of planetary cooling via mantle convection. Venus's surface indicates widespread volcanism and tectonism, with many distinct terranes, but in contrast to Earth, it remains a mystery how any or all of these features are connected to either each other or the underlying mantle dynamics (Smrekar et al., 2018; Adams et al., 2022; Widemann et al., 2023).

With the absence of plate tectonics on Venus, it is instead believed to be in a stagnant-lid regime, which is characterized by a strong conducting lid encircling the entire planetary surface (Solomatov, 1995). Convection occurs differently beneath a stagnant lid as heat flow out of a stagnant lid is limited, and mantle temperatures can remain higher over longer periods than their mobile lid counterparts. While the stagnant lid regime is most appropriate for the smaller, terrestrial bodies such as Mars, Mercury, and the Moon (Solomatov and Moresi, 1996; Thiriet et al., 2019), it has also been applied to Venus (Solomatov and Moresi, 1996, 1997; Reese et al., 1999a, b). In a stagnant lid planet, most of the potential temperature difference between the core–mantle boundary and the surface occurs across this thickened lithosphere, the upper-most extent of which is strong and does not actively participate in convection. Instead, a thin rheological

Correspondence to: M. C. Kerr, mkerr@ucsd.edu
Received 03 JUL 2024; Accepted 27 AUG 2024.
First Published online 06 SEP 2024.

sublayer at the base of the lithosphere generates small-scale instabilities in the form of cold drips (Solomatov, 1995). Due to the strong temperature-dependent viscosity of silicates, it's expected that the active region of the hot and cold thermal boundary layers have smaller viscosity ratios across them since the temperature drop across the active sublayer is merely a fraction of the total drop from the mantle to the surface (Jellinek et al., 2002). Rising mantle temperatures within a stagnant lid planet would in turn reduce the temperature jump, and its associated viscosity contrast, at the core–mantle boundary. In the case of Venus, topographic rises along the rims of some of Venus's largest coronae, such as Artemis and Quetzalpetlatl, might indicate lithospheric flexure which could arise from subduction (Sandwell and Schubert, 1992; Schubert and Sandwell, 1995; Davaille et al., 2017) or delamination (Adams et al., 2022, 2023). This would indicate Venus' lithosphere may not be perfectly stagnant, but that a limited amount of recycling might occur on a regional scale, which would not be inconsistent with interpretations of Venus' resurfacing history (Phillips et al., 1992).

In contrast, Earth is presently in a regime of whole mantle convection, with hot plumes rising from the core–mantle boundary (CMB), such as those underlying Iceland and Hawaii, and oceanic lithosphere (i.e. tectonic plates) recycling via subduction back into the mantle. The downwelling flows of colder, denser material associated with the history of subduction likely explain the long wavelength components of Earth's geoid (Lithgow-Bertelloni and Richards, 1998) and are thought to interact with chemically dense piles at the base of the mantle (McNamara and Zhong SJ, 2004, 2005). However, there is evidence via seismic tomography for descending slabs flattening or being deflected between depths of 660 km and 1000 km, indicating that some feature of the upper mantle may provide a barrier to flow for cold downwellings (Fukao and Obayashi, 2013; Faccenda and Dal Zilio, 2017).

Early studies focused on whether the phase transition of ringwoodite (ri) to bridgmanite (bg) plus ferropericlase (fp) could cause global layering of the mantle at 660 km depth (Christensen and Yuen, 1984), as this system was considered to have a strongly negative Clapeyron slope, ($\frac{\mathrm{d}P}{\mathrm{d}T}$), of −6 MPa/K. Subsequent measurements suggested the value was only −3 MPa/K (Ito and Takahashi, 1989; Irifune et al., 1998), which mantle convection models incorporated and reported that only weak or transient layering was possible (Tackley et al., 1993; Honda et al., 1993). Surface kinematics such as trench migration were also shown to play a central role in producing the observed layering of slab structures in the upper mantle (van der Hilst and Seno, 1993; Christensen, 1996), especially in combination with other factors such as the bending and sinking mechanics of cold slabs (Čížková et al., 2002; Goes et al., 2017) and mantle viscosity stratification (Yanagisawa et al., 2010).

More contemporary studies suggest the negative Clapeyron slope for a pyrolite composition in the upper mantle might be as weak as −1 MPa/K (Ishii et al., 2011, 2019) or −0.5 MPa/K (Litasov et al., 2005), which would imply the phase change has minimal effect and is therefore not consequential for the origin of slab deflection and flattening. However, recent studies of the Clapeyron slope for a harzburgite composition report a value of −3 ± 1 MPa/K (Ishii et al., 2018). As Earth's mantle has experienced a lot of melt extraction during its evolution, this larger Clapeyron slope may be more appropriate whereby pyrolite has been differentiated into a mechanical mixture that is predominately harzburgite (~80%) and basalt (~20%). The negative buoyancy of slabs in the mid-mantle could also be reduced by other effects such as the reduced kinetics of phase transitions within the coldest portions of slabs (King et al., 2015) or if the lower mantle itself is intrinsically denser due to enrichment of basaltic lithologies (Ballmer et al., 2015).

The question of what types of downwellings exist in Venus' interior, and if the mineral phase transitions that occur in Earth's upper mantle could possibly cause layering in Venus' mantle remains unresolved. Some studies have incorporated the effects of the the ringwoodite to bridgmanite transition in numerical models of stagnant lid convection, typically using values around −2.5 MPa/K (Armann and Tackley, 2012; Benešová and Čížková, 2012; Huang JS et al., 2013; Rolf et al., 2018; Uppalapati et al., 2020) and mantles with a Earth-like potential temperature of 1600 K. However, observed and computed mineral physics phase equilibria do not necessarily predict the same sequence of phase transitions to occur under warmer conditions for MORB (Hirose, 2002), forsterite (Ichikawa et al., 2014), and pyrolite (Stixrude and Lithgow-Bertelloni, 2022) compositions. For example, if a mantle with a pyrolite composition has a potential temperature that exceeds 1900 K, the associated adiabat crosses into a phase assemblage of wadsleyite, majorite and ferropericlase (WMF) and then into majorite + ferropericlase (MF) (Stixrude and Lithgow-Bertelloni, 2022; Dannberg et al., 2022). Thus, this sequence could be more relevant for understanding the dynamics of mantle convection within a stagnant lid planet such as Venus. A key attribute of the WMF phase assemblage is its negative thermal expansivity (Stixrude and Lithgow-Bertelloni, 2022; Dannberg et al., 2022). Accordingly, in the WMF reaction zone, hotter material has a lower proportion of the less-dense phase, wadsleyite, and becomes effectively denser and negatively buoyant with respect to ambient mantle, while colder material has a lower proportion of the denser phases of majorite and ferropericlase and effectively thermally expands into less dense, positively buoyant material. Building on recent work (Dannberg et al., 2022; Li RP et al., 2024), this study will investigate how mantle dynamics are affected by the presence of the WMF phase assemblage in numerical models of mantle convection with conditions appropriate for Venus.

2. Model Description

To investigate the effect of mineral assemblages predicted for warmer mantles under the conditions of a stagnant lid planet, we employ the geodynamic code ASPECT version 2.4 (Glerum et al., 2022), which can numerically model mantle convection in a 2D cylindrical annulus. We adopt the recently developed methodology for modeling phase transitions in thermal convection using the entropy formulation of the energy equation (Dannberg et al., 2022) and the projected density approximation (Gassmöller et al., 2020) which brings novel improvements to modeling sharp phase transitions and the effects of compressibility. This new methodology provides some advantages over previous approaches: 1) reformulating the energy equation in terms of entropy instead of temperature, so it becomes continuous at a phase boundary and constant along an adiabat; 2) using the projected density approximation (PDA) to avoid dynamic pressure effects on density to avoid oscillations in the solution while keeping the dynamic effects of temperature (Gassmöller et al., 2020); and 3) readily incorporating a precomputed mineral phase map for a pyrolitic mantle via a pressure-entropy look-up table generated by the HeFESTo software which computes phase equilibria and physical properties for mineral assemblages over the thermodynamic regime of Earth's mantle (Stixrude and Lithgow-Bertelloni, 2005, 2011). The entropy-based method employed in ASPECT allows the dynamic and latent heat effects of both sharp and broad phase transitions to be modelled accurately in a multi-phase assemblage. For more details on those respective methods, see Dannberg et al. (2022) and Gassmöller et al. (2020).

2.1 Mineral Phase Assemblages in Warmer Mantles

The equation of state for a pyrolitic mantle is defined by a look-up table, where pressure (P) and entropy (S) are independent variables generated by the Gibbs free energy minimization software HeFESTo (Stixrude and Lithgow-Bertelloni, 2005, 2011). The specific look-up table used in this study is the one provided in the supporting materials of Dannberg et al. (2022) for a bulk pyrolite equilibrium assemblage with 18% basalt and 82% harzburgite, (Xu WB et al., 2008). The table extends from 0–140 GPa in pressure and from 600–3600 J/K in entropy with a resolution in pressure of 100 MPa and 10 J/K in entropy. Figure 1 displays an example of some of the information contained in the look-up table which includes a) thermal expansivity and b) density, displayed here in pressure–temperature space. We also show variations in density due to temperature along lines of constant pressure (Figure 1c). For reference, Figure 1a also provides the adiabatic profiles for mantle potential temperatures between 1600 K to 1900 K in 100 K increments and these 4 adiabats are also displayed as dashed white lines in Figure 1b.

In Figure 1b we provide a simplified phase diagram denoting the dominant mineral phases overlying the density field. As can be seen in Figure 1b, descending along the adiabat in a mantle with potential temperature of 1600 K (or lower) represents the nominal transition zone of Earth between 13.5–23 GPa with a characteristic mineralogy dominated by olivine and its high-pressure polymorphs (wadsleyite and ringwoodite) with other minor phases present, before transforming into a bridgmanite dominated assemblage above 23 GPa. The warmer mantle adiabats each encounter different sequences and spatial durations of phase transitions between 12–25 GPa. Instead of a sharp transition into

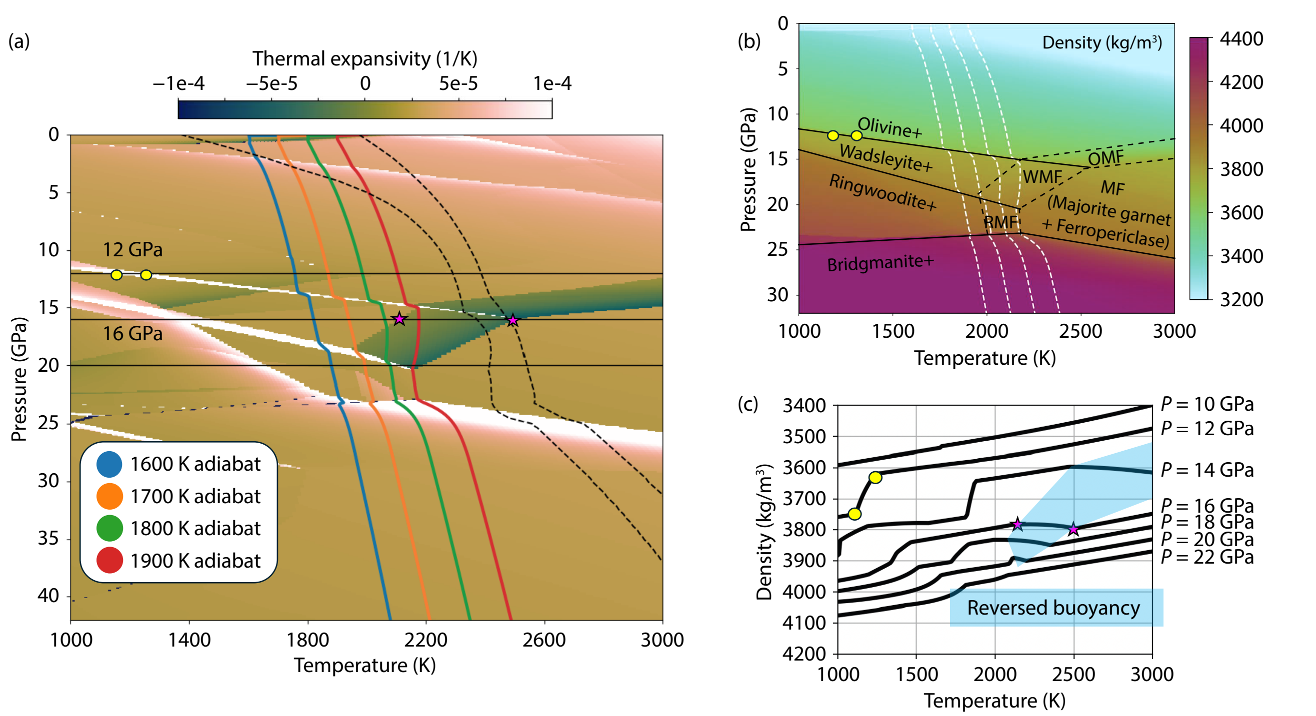

Figure 1. Pressure–temperature maps of (a) thermal expansivity (α) and (b) density (ρ) of the pyrolitic composition from Dannberg et al. (2022) overlaid with mantle adiabats for 1600 K, 1700 K, 1800 K, 1900 K and the anhydrous pyrolite solidus and liquidus (dotted black lines) from Stixrude and Lithgow-Bertelloni (2009). Plot (b) shows the major mineral phases and highlights the transitions between these phases in black. The beginning and end of the RMF, WMF, and OMF reaction zones are plotted in dotted black lines. Plot (c) shows density versus temperature relation along isobars. The light blue highlighted region indicates where increasing temperature at constant pressure increases the density in the WMF zone, demonstrating the negative thermal expansivity in effect at that region. The pink stars bound this zone of reversed buoyancy at 16 GPa and the yellow circles bound the olivine–wadsleyite transition at 12 GPa. The $ri = bg + fp$ transition can be seen as a kink in the 1600 K and 1700 K adiabats and as having an effective negative thermal expansivity (thin dark blue line around 24 GPa) as well. The expected negative temperature jump from $ri = br + fp$ is somewhat compensated by the positive temperature jump due to the $ri + st = gt$ transition, which has a positive coefficient of thermal expansivity across that reaction zone.

ringwoodite, the 1700 K adiabat crosses from wadsleyite into an assemblage of ringwoodite and majorite + ferropericlase (RMF) before converting to bridgmanite. However, the 1800 K crosses from the wadsleyite phase first into the WMF reaction zone, where the $wd = mj + fp$ transition takes place. Then it enters the RMF ($ri = mj + fp$) transition zone before transitioning to bridgmanite around 740 km deep. The 1900 K adiabat crosses from olivine into the thickest region of the WMF transition zone and then descends along the high temperature extent of the $ri = mj + fp$ transition (RMF zone) before transforming to bridgmanite. The phase map indicates that for the equilibrium pyrolite composition, majorite garnet + ferropericlase (MF) is stabilized at the higher temperatures across a broad range of pressures typically dominated by wadsleyite and ringwoodite at lower temperatures. Interestingly, there are extended regions where olivine, wadsleyite and ringwoodite form transitional assemblages, here labeled as OMF, WMF, and RMF, respectively, before reaching the MF stability field. However, the OMF region is minimally-existent due to its inhabiting the region in *T-P* above the anhydrous pyrolite solidus and liquidus. These intermediary mineral assemblages not only lie exactly within the pressure and temperature region of interest for this study, but also induce interesting mantle dynamics. For example, both OMF and WMF zones have effective negative thermal expansivity (white and blue region in Figure 1a) as well as WMF and RMF having ~30–40% larger specific heats (not shown).

The existence of broad regions containing mineral assemblages with effective negative thermal expansivity is quite interesting because the dynamics of mantle convection are largely understood as a competition between viscous resisting forces and driving forces arising from the buoyancy generated by sharp phase changes (e.g. $ri = bg + fp$) and the thermal expansion and contraction of mantle minerals which have positive coefficients of thermal expansivity. If these thicker transition zones exist in which the thermal expansivity is ostensibly negative, yet has similar magnitude compared to typical mantle materials, the dynamical effects would not be subject to the well-developed intuition from previous studies. As an example, with pressure held constant, mantle materials such as olivine would normally expand to an increase in temperature and become less dense. This is exactly the trend seen in the 10 GPa isobar of Figure 1c, in which the positive slope simply reflects the magnitude of thermal expansion. Changes in density can also occur due to phase transformations, as shown by the yellow dots in Figure 1a, b which indicate the temperatures along the 12 GPa isobar for where olivine has transformed into wadsleyite and an associated density jump occurs (Figure 1c). However, a negative slope along an isobar, as indicated by pink stars on the 16 GPa isobar in Figure 1c, indicates the typical sense of buoyancy is reversed, like at an endothermic phase transition with a negative Clapeyron slope. The combined effects of mantle compressibility, density jumps due to phase changes, and broad phase transition zones, where thermal expansion is effectively negative, can lead to interesting complexities when convective features pass through this pressure range. Consequently, the 4 values of initial mantle potential temperatures shown in Figure 1a essentially offer 4 different planetary mantles based purely on the predicted sequence of mineral phase assemblages and their associated thermodynamic properties.

2.2 Governing Equations of Thermal Convection

Entropy (S), pressure (P), and velocity ($\boldsymbol{u}$) are solved in a 2D cylindrical annulus using the projected density approximation (PDA) and entropy energy formulation employed in the finite-element geodynamic code ASPECT (Glerum et al., 2022). The system of equations for bottom-heated thermal convection are:

$$-\nabla\cdot(2\eta\dot{\varepsilon})+\nabla p=\rho_h\boldsymbol{g}, \tag{1}$$

$$\frac{\partial\rho_h}{\partial t}+\boldsymbol{u}\cdot\nabla\rho_h+\rho_h\nabla\cdot\boldsymbol{u}=0, \tag{2}$$

$$\rho_h T\left(\frac{\partial S}{\partial t}+u\cdot\nabla S\right)+\rho_h C_p\left.\frac{\partial T}{\partial t}\right|_{\mathrm{cond}}=2\eta\dot{\varepsilon}:\dot{\varepsilon}, \tag{3}$$

where variables are defined in Table 1, and $\rho_h = \rho(p_h, T)$ is the density which includes the effect of dynamic changes in temperature but uses the hydrostatic pressure to approximate density (Gassmöller et al., 2020). For this study we do not consider internal heating sources from radioactivity.

2.3 Temperature and Depth-dependent Viscosity

We model the mantle rheology as a Newtonian fluid with temper-

Table 1. Variables in thermal convection equations and their values.

Variable	Symbol	Value
velocity	$\boldsymbol{u}$	model solution (m/s^2)
temperature	T	from HeFESTo (K)
entropy	S	model solution (J/K)
pressure	p	model solution (Pa)
thermal expansivity	α	from HeFESTo (1/K)
specific heat capacity	C_p	from HeFESTo (J/kg/K)
viscosity	η	computed as reference profile (Pa·s)
gravity	$\boldsymbol{g}$	8.87 m/s^2
thermal conductivity	k	4.7 W/m/K
density	ρ	from HeFESTo (kg/m^3)
strain rate	$\dot{\varepsilon}$	model solution (1/s)

ature- and depth-dependence. The mantle viscosity in these models is the product of radially and laterally varying components, as formulated in Steinberger and Calderwood (2006). The radial component of viscosity, $\eta_{rad}(T_A, P)$, is based on the adiabatic mantle temperature profile, $T_A(r)$, and the hydrostatic pressure profile (P) using appropriate temperature- and depth-dependent values for an Arrhenius viscosity. Methods for incorporating this radial component of viscosity in the set-up for ASPECT models using the entropy formulation of convection is used in Li RP et al., (2024). This term is then multiplied by a factor representing the lateral temperature deviation from the adiabat, $\eta_{lat}(T_A, T)$ (Steinberger and Calderwood, 2006),

$$\begin{aligned}\eta(T,P) &= \eta_{rad}(T_A,P)\cdot\eta_{lat}(T_A,T)\\ &= A\exp\left[\frac{E_{act}+PV_{act}}{nRT_A}\right]\exp\left[-\frac{H_{lat}(T-T_A)}{nR(TT_A)}\right],\end{aligned} \tag{4}$$

where E_{act} = 2.4 × 10^5 J, n = 1 for a simple case of pure diffusion creep (Karato and Wu P, 1993), V_{act} is varied to generate different viscosity contrasts across the mantle as provided in Table 2, R is the gas constant, and A is the constant which defines the reference viscosity to be 10^{21} Pa·s at 1600 K and p = 0. H_{lat} is the activation enthalpy for the lateral variations in viscosity term where $H_{lat} = E_{act} + 23\times10^9\,V_{act}$ and where 23×10^9 Pa is a characteristic pressure corresponding roughly to the 660 km discontinuity on Earth. In practice, this viscosity law has both adiabatic temperature and pressure effects in the radial reference profile which are shown in Figure 2 as well as effects due to lateral temperature deviations from the initial adiabat which increase or decrease the viscosity at each depth. One parameter we varied is the degree of viscosity increase throughout the mantle. The parameter controlling this variation, V_{act}, was tuned for each radially-varying reference profile using the adiabatic temperature (T_A), pressure (P), and the

Table 2. Summary of initial conditions and variable rheological parameters.

Model	$T_{m,0}$ (K)	T_c (K)	S_c (J/K)	Viscosity contrast	V_{act} (m^3/mol)	max η (Pa·s)	$H_{lat}/(nR)$ (J)
ML1	1600	3177.97	2802.61	30×	1.84E-06	5.00E+22	33,950.59
ML2	1600	3177.97	2802.61	100×	2.05E-06	5.00E+22	34,548.65
ML3	1600	3177.97	2802.61	1000×	2.47E-06	5.00E+22	35,692.23
ML4	1700	3321.22	2858.38	30×	1.86E-06	5.00E+22	34,014.49
ML5	1700	3321.22	2858.38	100×	2.09E-06	5.00E+22	34,649.07
ML6	1700	3321.22	2858.38	1000×	2.53E-06	5.00E+22	35,861.66
ML7	1800	3486.9	2920.01	30×	1.92E-06	5.00E+22	34,170.78
ML8	1800	3486.9	2920.01	100×	2.16E-06	5.00E+22	34,846.58
ML9	1800	3486.9	2920.01	1000×	2.63E-06	5.00E+22	36,138.98
ML10	1900	3656.08	2980.34	30×	1.98E-06	5.00E+22	34,340.91
ML11	1900	3656.08	2980.34	100×	2.24E-06	5.00E+22	35,059.86
ML12	1900	3656.08	2980.34	1000×	2.74E-06	5.00E+22	36,434.69
SL1	1600	3177.97	2802.61	30×	1.84E-06	1.00E+25	33,950.59
SL2	1600	3177.97	2802.61	100×	2.05E-06	1.00E+25	34,548.65
SL3	1600	3177.97	2802.61	1000×	2.47E-06	1.00E+25	35,692.23
SL4	1700	3321.22	2858.38	30×	1.86E-06	1.00E+25	34,014.49
SL5	1700	3321.22	2858.38	100×	2.09E-06	1.00E+25	34,649.07
SL6	1700	3321.22	2858.38	1000×	2.53E-06	1.00E+25	35,861.66
SL7	1800	3486.9	2920.01	30×	1.92E-06	1.00E+25	34,170.78
SL8	1800	3486.9	2920.01	100×	2.16E-06	1.00E+25	34,846.58
SL9	1800	3486.9	2920.01	1000×	2.63E-06	1.00E+25	36,138.98
SL10	1900	3656.08	2980.34	30×	1.98E-06	1.00E+25	34,340.91
SL11	1900	3656.08	2980.34	100×	2.24E-06	1.00E+25	35,059.86
SL12	1900	3656.08	2980.34	1000×	2.74E-06	1.00E+25	36,434.69
SL13*	1900	3656.08	2980.34	30×	1.98E-06	1.00E+25	34,340.91
SL14*	1900	3656.08	2980.34	100×	2.24E-06	1.00E+25	35,059.86

Notes: * = linear smoothing of log[viscosity] profile through 10–30 GPa. The corresponding entropy used to set the temperature boundary condition at the core is determined using the look-up table at a pressure of 119 GPa and linearly interpolating between the entropy values which bound the desired temperature. Due to the differences in density structure between models with varying potential temperatures, the pressures at the CMB are 119.39 GPa, 118.98 GPa, 118.62 GPa, and 118.22 GPa for the 1600 K, 1700 K, 1800 K, and 1900 K mantles; respectively. Using the pressure of 119 GPa to interpolate the fixed entropy value for the CMB introduces a maximum variation between desired and actual temperatures at the core of −7.32 K.

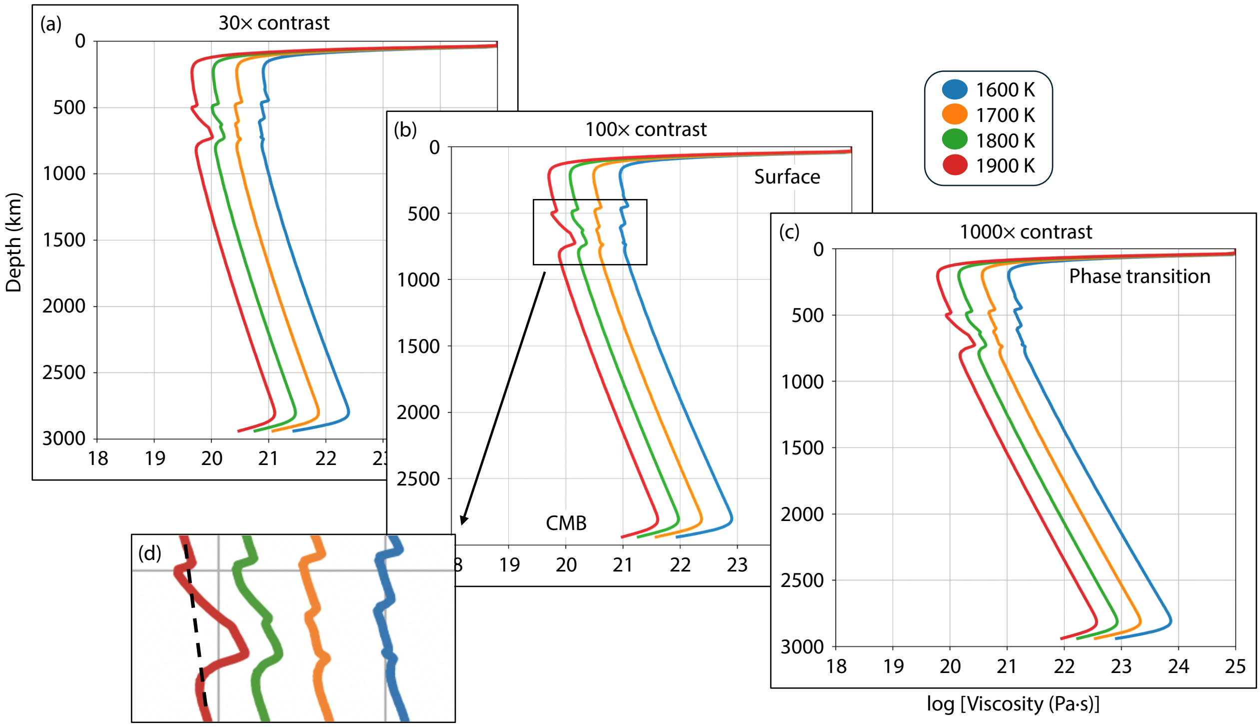

Figure 2. The initial viscosity profiles for models with potential temperatures of 1600 K, 1700 K,1800 K, and 1900 K with varying depth-dependence. Each model has a V_{act} value selected to generate an increase over the depth of the mantle of (a) 30×, (b) 100×, and (c) 1000×. In (d) the initial viscosity profiles through the mantle transition zone show a high viscosity ledge at approximately 700 km depth for the 1900 K profile. The black dashed line in (d) indicates the linear smoothing from 10–30 GPa applied to the initial viscosity profiles of SL13 and SL14.

Arrhenius viscosity law in Equation (4) such that the ratio between the reference surface viscosity and CMB viscosity was 30 (weak), 100 (moderate), or 1000 (extreme).

It is worth noting here that the viscosity profiles in Figure 2 differ in shape from those in Steinberger and Calderwood (2006) due to our using a constant activation volume and activation energy in the radially varying factor of our viscosity law, whereas they compute the activation enthalpy for the lower mantle from the shape of the melting temperature profile T_m with depth. This results in our profile having positive curvature in log-space and theirs decreasing in curvature with depth. The viscosity structure of Venus is relatively unconstrained, and our span of profiles explored a variety of convection efficiencies between the lower and upper mantle. We do not include a viscosity jump of ~10 at the $ri = bg + fp$ transition, even though such a jump is preferred for present-day Earth models. Conversely for Venus, Steinberger et al. (2010) found that the observational constraints of the high correlation between gravity and topography in the degree range of l = 5–40 are consistent with a high dynamic flow contribution to gravity and topography and a lack of a sharp viscosity increase in the mantle transition zone. Additionally, the absence of an Earth-like low viscosity zone in the upper mantle for our Venus-like models is consistent with constraints from geoid and topography observations at Venus's volcanic highlands, considered to be surface expressions of mantle plumes (Kiefer and Hager, 1991).

Another varied parameter besides the activation volume was the maximum viscosity, which controls the strength of the lithosphere by defining the extent of the rigidity for the coldest lithospheric material. What we define as mobile-lid models are those with a maximum viscosity of 5 × 10^{22} Pa·s, as used for Earth models in Dannberg et al. (2022), which is low enough to allow for the entire lithosphere to become unstable and sink. For stagnant-lid models, a maximum viscosity of 1 × 10^{25} Pa·s was sufficient to ensure the lithosphere was entirely rigid.

2.4 Initial and Boundary Conditions

We adapted the Earth models of Dannberg et al. (2022) into Venus models by setting the core radius R_{core} = 3110 km, the planetary radius to R_{planet} = 6052 km, and the gravity to g = 8.87 m/s^2. Figure 3 shows a summary of the initial conditions and boundary conditions for both the mobile lid (right side) and stagnant lid (left side) models. For both types of models, the inner and outer circular boundaries are free-slip and fixed-temperature, with the temperature enforced by fixing the value of entropy at surface and CMB pressures. The surface entropy is fixed at 1602.822 J/K, corresponding to Venus's surface temperature of 740 K. The mantle's initial state follows along an adiabat that starts with a potential temperature at the surface, ranging between 1600 K and 1900 K. This initial temperature field is computed by finding the entropy (S) corresponding to the desired potential temperature at the surface (T_0) and using the HeFESTo table to compute at each pressure in the mantle the corresponding temperature such that the entropy is constant (i.e. an adiabat). The temperature of the core is fixed to be 600 K hotter than the initial adiabatic temperature at the base of the mantle. Table 2 provides a summary of the initial conditions and boundary conditions used, and both the core temperatures and the corresponding entropies used to set those

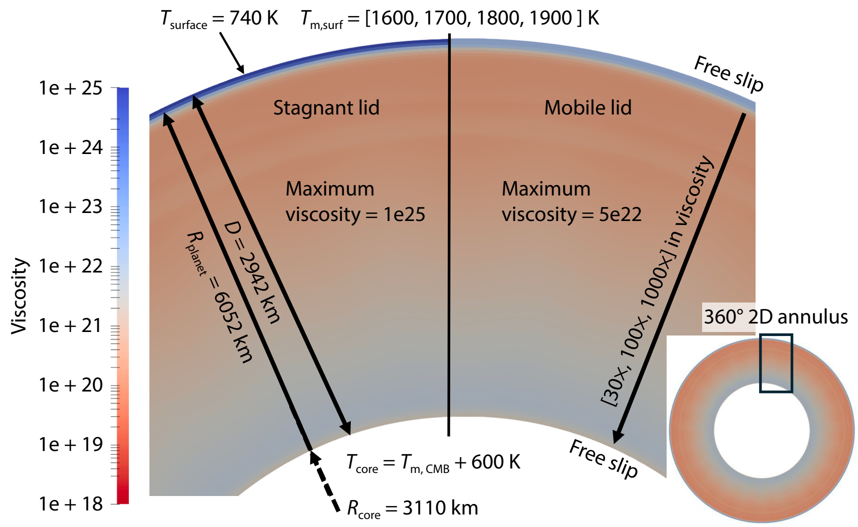

Figure 3. A summary of the initial conditions, boundary conditions, and geometric constraints of the problem in the initial viscosity field for an 1800 K mantle with 100× viscosity increase through the domain. The stagnant lid models (left) and mobile lid models (right) have a maximum viscosity of 10^{25} Pa·s and 5×10^{22} Pa·s, respectively.

temperatures are provided. At both the surface and core boundaries, the entropy of the mantle's interior smoothly transitions to these fixed boundary entropies using a half-space cooling model with an age of 50 Myrs. An initial sinusoidal perturbation is also prescribed in the entropy field with a 10 J/K magnitude and l = 23 wavelength with the intent of not introducing any persistent long-wavelength features into the mantle dynamics as the system evolves through an initial transient state. The initial radial resolution of rectangular finite elements is 128 cells and the angular resolution is 1536 cells.

2.5 Model Geometry

Due to computational limitations and the aim of conducting an exploratory study of the conditions under which upper mantle mineralogy affects convection, models were run in a 2D cylindrical geometry instead of 3D spherical geometry. One drawback of using 2D cylindrical geometry, is that both plumes and avalanches are sheets and divide the computational domain, whereas in 3D there is a more natural asymmetry of cold, downwelling sheetlike structures and hot plumes with radially-extending, axisymmetric conduits. The different surface area to volume ratios is also an issue when comparing heat fluxes with 3D spherical models as 2D annuli geometries can underestimate core heat flux and overestimate surface heat flux (van Keken, 2001; Fleury et al., 2024). The core and planetary ratios can be re-scaled so that heat fluxes are more comparable with 3D spherical geometry (van Keken, 2001), but for the case of stagnant lid models that are predominantly heated from below, the scaling does not greatly improve the accuracy (Fleury et al., 2024). Additionally, using 2D annulus geometry reduces crowding of upwelling features in the lower mantle compared to using an artificially smaller core. Although utilizing a 2D spherical annulus geometry (Hernlund and Tackley, 2008) can further mitigate some of these issues, for bottom-heated stagnant lid convection it only marginally improves scaling to 3D spherical geometry compared to 2D cylindrical (Fleury et al., 2024). However, ASPECT is currently limited to cylindrical geometry in 2D. It is possible that the cold drips in our 2D models are thinner and faster than equivalent features within a 3D spherical mode whereas hot plumes in 3D are observed to be hotter, faster, and thinner than their 2D cylindrical counterparts in sheet-form (Fleury et al., 2024).

3. Results

In order to investigate the effects of the varying mineral assemblages expected for warmer mantles under the conditions of both a stagnant lid and mobile lid, we produced two nearly identical suites of mantle convection models (of 12 models each). The main difference between the two suites' designs is the maximum viscosity of the lithosphere, which either allows for recycling or remains rigid. The range of mantle potential temperatures explored corresponds to a gradual stepping through of warmer scenarios in increments of 100 K, starting from an Earth-like mantle temperature of 1600 K. Another parameter of interest is the degree of radial viscosity stratification over the depth of the mantle, because it is also known to considerably influence mantle dynamics. The suites encompass three variations which can be characterized as weak (10×), moderate (100×), or extreme (1000×). A final two models were included to isolate the effect of viscosity variations due to the dependence of the radial viscosity term in Equation (4) on sharp features of the adiabatic temperature profile through the transition zone, appearing prominently in the 1900 K models (Figure 2d).

3.1 Mobile Lid Convection

For all mobile lid models the entropy perturbation in the initial condition leads to an initial system of 23 upwellings and downwellings which become unstable once the local Rayleigh number at these boundaries exceed the critical value needed to transition from conductive to convective heat flow. The local Rayleigh number is dependent on viscosity, so the time until the first hot plumes are generated at the core is longer for more viscous lower mantles.

The transient stage of convection at model onset generates a rapid increase in mean surface heat flux as cold plumes form and sink rapidly due to their negative thermal buoyancy, replacing the cold material with warmer ambient mantle. This is followed by an increase in the core heat flow corresponding to the generation of a large thermal gradient across the CMB due to the accumulation of cold material from the initial downwellings. The thickness of the cold thermal boundary layer in our mobile lid model varies regionally: thicker around the conduits of descending plumes and thinner above the heads of ascending hot plumes, which heat the base of the lithosphere and also laterally displace the mobile lithosphere towards the downwelling conduits. As the system evolves towards a steady state, the number of large upwellings and downwellings reduces as plumes merge and the system relaxes into its natural wavelength of convection.

Figure 4 shows a characteristic evolved state for mobile lid models with mantle temperatures evolving from intial values of 1600–1900 K and a viscosity profile with a 100× increase through the mantle. In the 1600 K and 1700 K models, there is little evidence that mantle phase transitions influence convection dynamics, as upwellings and downwellings pass through the transition zone unimpeded. In the 1800 K model, downwellings passing through the WMF region appear to consistently "pinch" within that layer, becoming thinner downwellings in the lower mantle. The 1900 K model exhibits the pinching of subducting downwellings as well. They also exhibit a mixture of large, voluminous downwellings with some smaller sub-lithospheric drips (also see ML10 in Figure 7) away from the main downwelling conduits resulting in some ephemeral layering. The smaller drips accumulate at a depth between 500–600 km and are flushed from the upper mantle when a larger, cold downwelling penetrates the transition zone or when a downwelling laterally drifts across the surface (akin to rollback subduction) and entrains the ponded material into the lower mantle. These accumulations of smaller drips are flushed by larger downwelling flows on timescales that are mostly, but not always, faster than they can generate their own instability (Figure 7, ML10).

In models with 1000× radial viscosity stratification (not shown), instabilities from the hot thermal boundary layer take more time to gain sufficient buoyancy force to push through the lower mantle. As a result, these models tend to have fewer, larger plumes from having spent a prolonged time accumulating boundary layer fluid or needing to coalesce with adjacent plumes to punch through the high viscosity barrier. The most voluminous cold downwellings directly from the lithosphere pass through the mantle transition zone without stagnation or layering, mixing the entirety of the mantle.

3.2 Stagnant Lid Convection

Figure 5 shows a characteristic evolution for bottom heated stagnant lid models with mantle temperatures of 1600–1900 K (models SL1–12) and corresponding CMB temperatures 600 K hotter than the real temperature at the base of the adiabat. Each model evolves into steady state from an initial state of 23 hot and cold downwellings, which, under stagnant lid conditions, produces sub-lithospheric drips spaced ~100 km apart with small plume heads and thin trailing conduits. A systematic pattern across the model suite is the presence of inherent asymmetries related to the hot and cold instabilities rising from the respective thermal boundary layers. Instabilities from the stagnant lid (cold drips) are largest in the 1600 K models. With increasingly warmer mantles, the cold drips gradually decrease in size and increase in number and frequency. On the other hand, the number and frequency of hot plumes seem less dependent on mantle potential temperature and more dependent on the degree of viscosity increase with depth. Larger viscosity contrasts result in thicker, hotter plumes; however the number and size of cold drips is nearly independent of radial viscosity stratification for models of a given potential temperature. In general, our bottom-heated stagnant lid models with some degree of radial viscosity stratification exhibit an inherent asymmetry in which there are typically many more cold drips than hot plumes, and the hot plumes are larger and stronger than the cold drips.

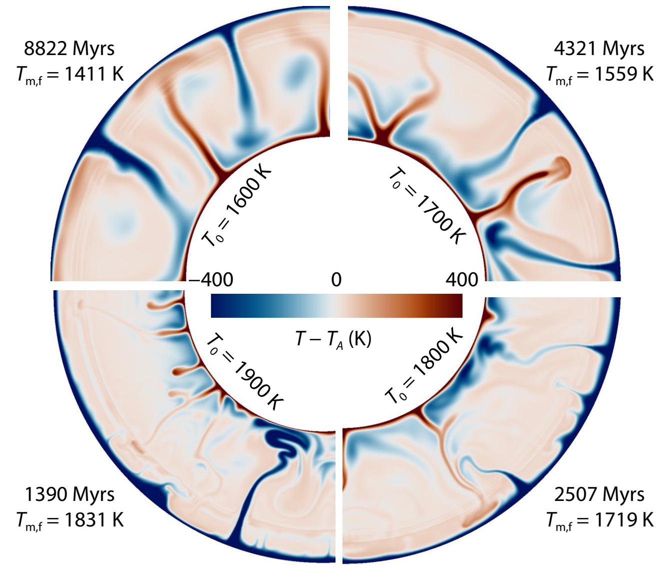

Figure 4. Snapshots of non-adiabatic temperature for mobile lid models ML2, ML5, ML8, and ML11 (clockwise from the top left) at steady states of their evolution. The final mantle potential temperatures of these models are $T_{m,f}$ and show the overall cooling trends of these mantles with no radioactive heat generation.

Across the stagnant lid suite, the 1600 K models have the lowest Rayleigh numbers and thickest lithospheres, resulting in the largest instabilities generated from the thermal boundary layers. These models also have the coldest mantle potential temperature of the suite and at no point does the mantle adiabat cross through the WMF phase region, and unsurprisingly the models do not exhibit any mantle layering. For the 1700 K mantles, the warmer up-welling material appears trapped in and above the transition zone, notably for the 30× and 100× cases of the 1700 K model which see their average mantle temperatures increase over time. As these mantles get warmer, the temperatures of the lithospheric drips migrate into the WMF zone and are deflected and weakened before entering the lower mantle. The 1800 K models exhibit this behavior to a greater degree as some drips within 100 K of the 1800 K adiabat start to become less dense from

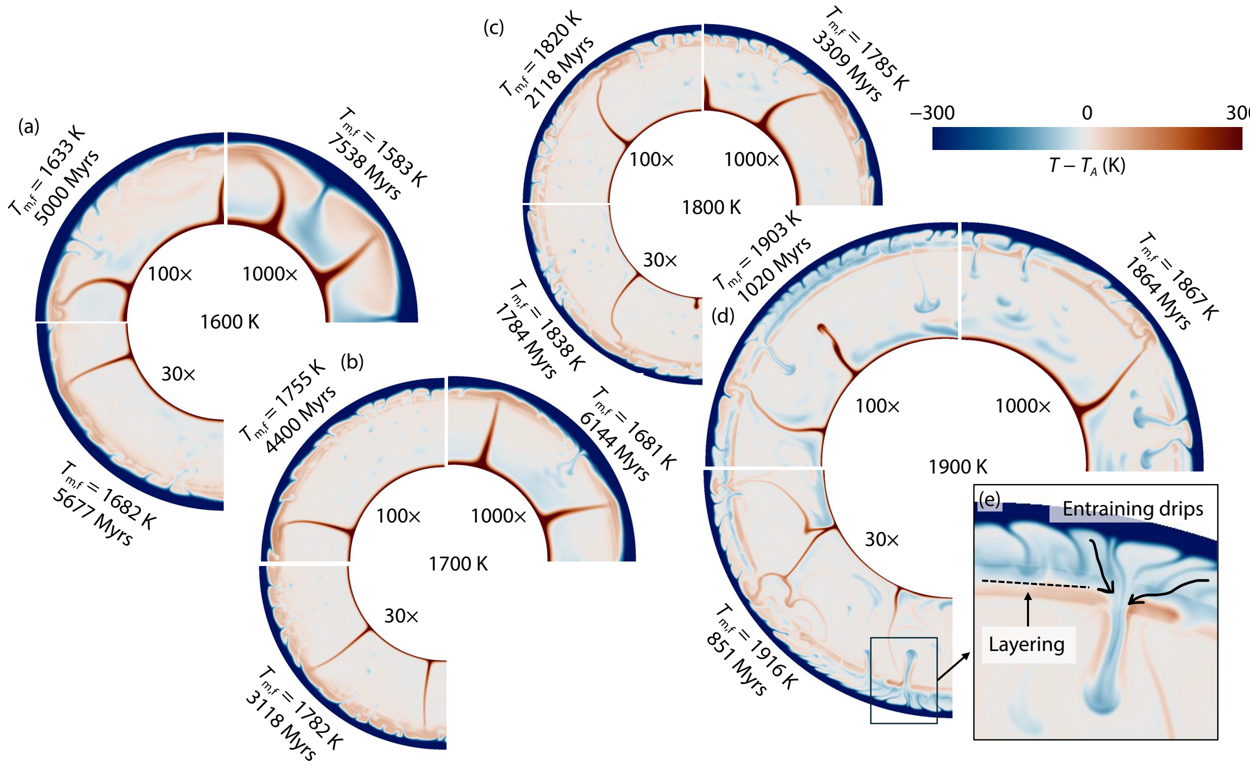

Figure 5. Snapshots at the final time step of stagnant lid models SL1–12 representing the non-adiabatic temperature field of models with initial potential temperatures of (a) 1600 K, (b) 1700 K, (c) 1800 K, and (d) 1900 K and mantle viscosity ratios of 30, 100, and 1000. The zoomed-in panel (e) shows layering at the base of the WMF region at ~600 km depth and cold drips from the lid entrained by the conduit of a mantle avalanche.

reduced amounts of majorite and ferropericlase (Figure 1b). Still, these cold drips from the lithosphere, which see some degree of deflection, otherwise pass through to the lower mantle and do not layer (Figure 5c). The presence of the phase transition in the upper mantle of the 1700 K and 1800 K stagnant lid models traps material from the up-welling plumes, increasing the temperature in the upper mantle between 20–100 K globally with respect to the adiabatic profile.

For the stagnant lid models with a temperature of 1900 K, there were no large cold downwellings originating from the cold thermal boundary layer that could individually penetrate the mantle transition zone. The buoyancy of both hot and cold downwellings are weakened by the phase transition into the WMF phase assemblage. Since hot plumes are larger and stronger than the cold drips, having had to push through the higher viscosity material in the lower mantle, they pass through the phase transition. Conversely, the sub-lithospheric drips layer between 500 km and 600 km depth. The layering is ephemeral, and all the accumulated material from the cold drips descend into the lower mantle as mantle avalanches, finally accumulating at the core mantle boundary. This is in contrast to the mobile lid models where some mantle avalanches could occur in the 1900 K models; however, in stagnant lid 1900 K models, avalanches are the dominant mode of whole mantle downwellings. A summary of whether or not avalanches were observed in our models is provided in Table 3.

3.3 Melting

Each model was assessed a posteriori with regards to the degree of potential partial melting, even though melting is not implemented in our models. Attention was particularly given to those with the hottest initial mantle temperature of 1900 K and within the mantle transition zone where the effects of partial melting are likely to have more consequential dynamic effects than the reversed buoyancy effects of the WMF reaction zone. The temperature field of the model was compared to the solidus and liquidus of dry pyrolite as computed in Stixrude and Lithgow-Bertelloni (2009) for all points in the domain, and melt fraction was computed according to

$$\phi = \frac{(T - T_{\mathrm{sol}})}{(T_{\mathrm{liq}} - T_{\mathrm{sol}})}.$$

It was found that for all models, there was no partial melting in the mantle transition zone or anywhere in the model at pressures greater than ~5 GPa. For the 1800 K and 1900 K mobile lid models, the thinning of the lithosphere due to its lower viscosity and susceptibility to flow allows for hotter ambient mantle material to be present at lower pressures, and regional partial melting occurs above ~5 GPa away from the large mantle downwellings. For the stagnant lid models, there was no partial melting in the 1900 K model with an extreme viscosity contrast.

3.4 Mantle Avalanche Dynamics

For models with a 1900 K initial potential temperature, cold drips from the thin rheological sublayer of a stagnant lid planet begin to stall and pond upon reaching the MF edge of the WMF reaction zone at 600 km depth (Figure 5e, black dashed line). Because the

Table 3. Summary of model results.

Model	Mantle avalanches (Y/N)	t_f (Myrs)	$\Delta T_{m,f}$ (K)	$\Delta\bar{T}/t_f$ (K/Gyr)	$\bar{q}_{surf}$ (mW/m^2)	$\bar{q}_{core}$ (mW/m^2)
ML1	N	7034	−133	−26.0	32 ± 13	61 ± 25
ML2	N	8822	−189	−27.9	36 ± 16	61 ± 28
ML3	N	6864	−218	−40.0	36 ± 23	56 ± 26
ML4	N	2945	−66.1	−33.5	45 ± 13	73 ± 31
ML5	N	4321	−141	−44.4	38 ± 13	61 ± 24
ML6	N	8087	−242	−39.3	35 ± 17	67 ± 30
ML7	N	1567	−26.1	−28.3	61 ± 21	89 ± 50
ML8	N	2507	−80.5	−48.2	51 ± 21	64 ± 23
ML9	N	4164	−206	−64.6	47 ± 19	66 ± 30
ML10	Y (some)	964.2	−29.2	−59.0	72 ± 28	109 ± 44
ML11	Y (some)	1391	−69.2	−78.1	65 ± 30	83 ± 38
ML12	Y (some)	2000	−149	−94.0	61 ± 23	56 ± 26
SL1	N	5677	81.6	8.80	13 ± 1	33 ± 9
SL2	N	5000	33.2	−4.24	11 ± 3	25 ± 7
SL3	N	7538	−16.2	−11.63	10 ± 3	19 ± 6
SL4	N	3118	81.8	22.2	19 ± 2	38 ± 8
SL5	N	4400	55.2	5.76	16 ± 2	28 ± 6
SL6	N	6144	−18.3	−13.4	12 ± 2	23 ± 6
SL7	N	1784	38.3	12.4	23 ± 3	58 ± 13
SL8	N	2118	20.0	−3.66	21 ± 2	41 ± 9
SL9	N	3309	−15.7	−19.3	17 ± 3	25 ± 6
SL10	Y	836.9	15.6	−2.94	33 ± 3	78 ± 23
SL11	Y	1020	2.8	−25.4	30 ± 3	62 ± 17
SL12	Y	1864	−32.2	−42.7	23 ± 4	37 ± 10
SL13*	Y	722.6	15.7	−6.08	33 ± 3	78 ± 23
SL14*	Y	847.7	2.8	−29.4	30 ± 3	59 ± 21

Notes: t_f, final time; $\Delta T_{m,f}$, rate of change in volumetrically averaged mantle temperature across the entire evolution; $\Delta\bar{T}/t_f$, change in mantle potential temperature as computed from mid-mantle entropy; $\bar{q}_{surf}$, final average surface heat flux; and $\bar{q}_{core}$, final average core heat flux. * = linear smoothing of log[viscosity] profile through 10–30 GPa.

1900 K adiabat passes through WMF zone, the effective negative thermal expansivity renders cold material less dense than mantle material below it, allowing it to rest atop the MF-dominated edge of the WMF reaction zone. Subsequent generations of cold drips from the thermal boundary layer accumulate on top of the cold trapped material from the initial downwellings, as seen in Figure 5e.

The avalanche initiates when the cold, positively buoyant material trapped within the WMF zone is pushed far enough downward by some driving force that it leaves the zone of negative expansivity and regains its negative buoyancy. The driving force to initiate an avalanche can come from directly above the layer or laterally. When enough cold material has accumulated and ponded above the negative expansivity zone, producing a regional net-negative buoyancy, the bottom portion of the stalled layer is pushed past the WMF-MF edge and descends. Alternatively, initiation of avalanches can be related to lateral forces driven by adjacent convective motions. Material within the zone of reversed buoyancy is confined within the region between the wadsleyite-dominated and Majorite + Ferropericlase-dominated edges of the WMF zone by hot ponded material on the MF side and cold ponded material on the olivine side. Hot plumes penetrating the WMF zone can displace the trapped material by forcing it to move either laterally or vertically down, generating an unstable perturbation at the WMF-MF edge and forcing some amount of trapped cold material to pass downwards through the WMF-MF edge. Its ”normal” negative buoyancy is then restored to reinforce the larger scale avalanche instability.

The avalanche conduits are cut off as the upwards force of positively-buoyant cold material in the WMF zone competes with suction of entrained upper mantle material that flows laterally towards a smaller conduit of downwelling flow. In the 1000× models, some conduits start thicker since the downwelling velocity through the lower mantle is slower and material has enough time to laterally entrain into the conduit. However, this thickness is short-lived since the slow descent results in less entrainment velocity through the WMF zone for material coming through that pathway. The slowing of lateral flow allows the system to more quickly revert back to a state of stagnation, corresponding to avalanches that flush sooner. Additionally, fewer plumes from the CMB, due to the suppressing effect of high viscosity at depth, generate fewer perturbations on the boundary which means each avalanche has the potential to entrain more material individually than if there were many perturbations. Thus, there is a complex dependence of the sizes of the avalanches on the timing, distribution, and number of hot plumes ascending as well as on the past timing, distribution, and number of recent avalanches.

The forces driving the dynamics of the mantle transition zone can be investigated by looking at the estimated buoyancy field in the upper mantle. Changes in the volumetric buoyancy force B are driven by temperature variations from a reference adiabatic temperature T_A. The adiabatic temperature profile and densities along that curve are interpolated from the S-P look-up table at each time step corresponding to the mean entropy of the mantle between 30 and 90 GPa. The estimated thermal buoyancy field is given by

$$B_{\mathrm{est}} = \rho_A \alpha g \left(T - T_A\right) \tag{5}$$

and represents the effective volumetric force at a given point due to the local temperature, the reference adiabat, and the thermal expansivity. We regard this expression as an estimate because the applied thermal expansivity α is limited by the resolution of the look-up table, so for especially thin phase transitions, like the ringwoodite to bridgmanite + ferropericlase transition, the effective negative expansivity is under-resolved as an interpolated value (Figure 1a), even though its effects are accounted for in the density field which is used in the entropy equation (Equation (3)) and thus recorded dynamically in the model. The layering effects of interest are the thicker reaction zone of $wd = mj + fp$ which is better resolved in α and which we observe to induce more layering than the $ri = bg + fp$ transition which has a shallow Clapeyron slope of ~−1.4 MPa/K.

In Figure 6, the models SL2, SL5, SL8, and SL11 are plotted in the estimated thermal buoyancy field and the color scale is split according to the sign of the thermal expansivity as interpolated from the look-up table. Most of the mantle fluid shown in Figure 6 has a normal buoyancy by virtue of the minerals having a positive thermal expansion coefficient. Cold material becomes denser due to thermal contraction (green) and warm material becomes less dense due to thermal expansion (magenta). However, in the 1800 K model (Figure 6c), the hot up-welling plume becomes negatively buoyant (purple) in the WMF zone and deflects laterally instead of all the plume material rising directly upward. Similarly, in the 1900 K model (Figure 6d), the cold drips from the lithosphere (highlighted with black circles) are seen entering the mantle transition zone as green and progressively transforming to orange (positively buoyant with negative thermal expansivity), implying the force on the drip changed from radially downwards to upwards. The reversal of buoyancy occurs across the depth of the WFM phase assemblage but is stronger at its base. Within the root of an avalanche conduit (Figure 6d, leftmost black circle), material experiencing a reversed sense of buoyancy force (in orange) actually wants to rise but is viscously coupled to the downwelling material beneath it. As the downwelling flow is larger, it provides an overwhelming amount of negative buoyancy and successfully entrains the positively buoyant cold material down with it.

Once a perturbation has progressed far enough that a sufficient amount of previously trapped cold material has had its negative buoyancy restored, an avalanche develops which is a composite

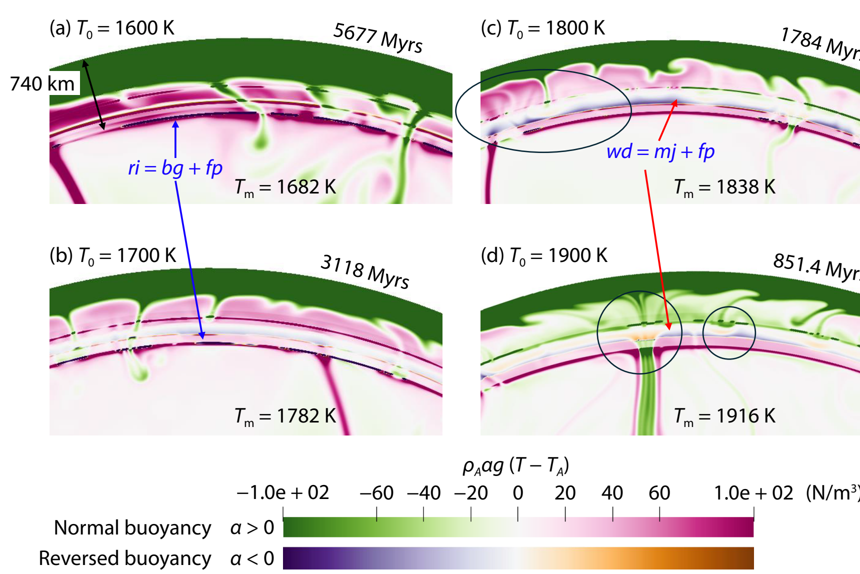

Figure 6. Upper mantle region of stagnant lid models (a) SL1, (b) SL4, (c) SL7, and (d) SL10 showing estimated buoyancy of mantle with respect to the adiabatic mantle. For material with non-adiabatic temperatures that pass into the WMF transition region, the associated negative thermal expansivity ($\alpha < 0$) makes the buoyancy opposite to normal mantle behavior (shown with the purple-orange color bar). Location of the $ri = bg + fp$ phase transition at 740 km is labeled as well with an effective negative coefficient of thermal expansivity shown in Figure 1a. Circled features indicate regions where (c) upwellings and (d) downwellings transition through the zone of reversed buoyancy.

downwelling that is considerably larger than the individual cold drips from the lithosphere. As it sinks into the lower mantle, it can entrain remaining adjacent cold material with it, even if that material is otherwise neutrally- or positively-buoyant in the WMF zone. These dynamics are shown in the left-most circled region of Figure 6d.

3.5 Mantle Avalanches and Heat Flow

Due to the increased mobility of cold material in a mobile lid model, these models cool more efficiently since a greater volume of mantle material is able to convect. Two-sided symmetric downwellings thin the lithosphere and allow greater surface heat flow despite the core heat flows of stagnant-lid and mobile-lid being more similar. Mobile lid models cool at rates between 25–95 K/Gyr. On the other hand, stagnant-lid planets cool very slowly due to the presence of an immobile conductive lid that traps heat inside the planet, and in some cases actually warms up because the bottom heating exceeds the cooling through the surface. The temperature change over time of the stagnant lid planets is more variable with most models cooling 5–45 K/Gyr, but 4 models heating up at rates of 5–22 K/Gyr. Variability between models of a similar lithospheric rigidity appears to be controlled by the degree of radial viscosity stratification and initial mantle temperature. Models with 1000× viscosity increase with depth suppress plume generation at the CMB, which reduces the associated heat flow from the core and leads to highest rates of mantle cooling. The presence of mantle avalanches might increase the overall cooling of the planet for SL10–14. Models with weak radial viscosity stratification (30×) such as SL1, SL4, and SL7 all heated up at 8.8 K/Gyr, 22.2 K/Gyr, and 12.4 K/Gyr, respectively. However, the model SL10 (also 30×) actually shows the opposite and cools at −2.9 K/Gyr. Similarly, for models with moderate radial viscosity stratification (100×), SL5 is warming but SL2 and SL8 are both cooling at −4.24 K/Gyr and −3.66 K/Gyr, respectively, while SL11 is cooling much faster at −25.4 K/Gyr. It seems in both cases the models with avalanches are cooling disproportionately faster for having only a slightly warmer mantle. Although mantle cooling in SL10 and SL11 could be enhanced by having a slightly different stagnant lid thicknesses than the other models, in particular during the earlier stages of the systems thermal evolution, the mantle avalanches considerably enhance large scale stirring of the interior which counters the natural thermal stratification of hotter material in the upper mantle of stagnant lid models. The enhanced cooling rates may be a byproduct of the increased thermal mixing of the interior.

3.6 Radial Viscosity Variations in the Transition Zone

The mantle adiabats for the 1800 K and 1900 K models exhibit departures from the expected quasi-linear increase with depth due to thermodynamic effects of the WMF phase transition, causing the mantle to get slightly colder with depth instead of warmer (Figure 1a, b). These departures actually cause a corresponding increase ("bump") in viscosity of about a factor of 4 over the 600–750 km depth range (Figure 2d). We designed two models (SL13 and SL14) in order to test whether or not this bump in the radial viscosity profile was the singular reason for the ephemeral layering at 600 km depth in the 1900 K stagnant lid models. For these models, all parameters and initial conditions were identical to those in models SL10 and SL11 except for a linear smoothing of the viscosity through the region of the bump (dashed black line in Figure 2d). In Figure 7 we show the results of this test with a side-by-side comparison of SL13 with its twin SL10, as well as the mobile lid version ML10 for reference. There are no distinguishable differences in mantle avalanche formation between models SL10 and SL13 due to the presence or absence of a bump in the radial viscosity profile in the transition region.

From this result we can conclude that the ultimate cause of layering at the WMF-MF phase boundary is due to the thermodynamic properties of the WMF mineral assemblage and not because of the bumps in radial viscosity. Furthermore, model ML10 exhibits ponding of small, cold drips that lead to ephemeral layering atop the WMF-MF phase boundary, as well as a noticeable pinching of larger downwellings that eventually pass through the WMF-MF phase boundary. Some of the lower mantle downwellings in ML10 (and ML11–12, not shown) are clear, archetypical mantle avalanches, forming when there is not a substantial amount of mass exchange from large cold lithospheric downwellings keeping the system well-mixed. It happens that for ML10, the large downwelling in the snapshot in Figure 7 is the only lithospheric downwelling in the entire model domain, generating a global asymmetry in mantle convection dynamics. Drips build up and avalanche on their own time scale due to a lack of consistent lithospheric downwellings to disrupt the layering. However, it can be generally said that for mobile lid models, the dominant form of mantle downwelling is a cold voluminous plume from the lithosphere, and for stagnant lid models at or above 1900 K, the dominant, and only mode of lower-mantle downwelling is a mantle avalanche.

4. Discussion

This work follows directly from research conducted in Dannberg et al. (2022) where the entropy method was first formulated and used. That study used Earth-like geometries and boundary conditions and explored mantle temperatures of 1600 K, 1700 K, and 1800 K. In their 1800 K models, some layering of hot plumes at the transition region was noted, and it was implied that an early Earth could exhibit mantle layering and the stagnation of hot plumes at the upper mantle. The work of Ichikawa et al. (2014) had previously investigated hot plumes at the WMF-MF transition in a mobile lid regime in the context of an early Earth, and they primarily report increased plume temperatures as much as 100–150 K due to latent heat release from MF to WMF phase change. A more recent study (Li RP et al., 2024), also within the mobile lid regime, expanded the range of mantle temperatures to include 1900 K with additional consideration of the effects of internal heating. Li RP et al. (2024) identify a layering regime in which the WMF to MF phase transition impedes up-welling plumes in models with mantle temperatures 1900 K, as long as the system has not experienced enough secular cooling through thermal evolution such that the mantle adiabat no longer crosses into the WMF region. We observe similar behavior in our mobile lid models with warmer initial mantle potential temperatures (>1800 K) while the mantle adiabat crosses into the WMF region (these models cool at an approximate rate of 50–100 K/Gyr). In particular, for the 1900 K models, deflection and stalling of hot plumes, as well as ponding

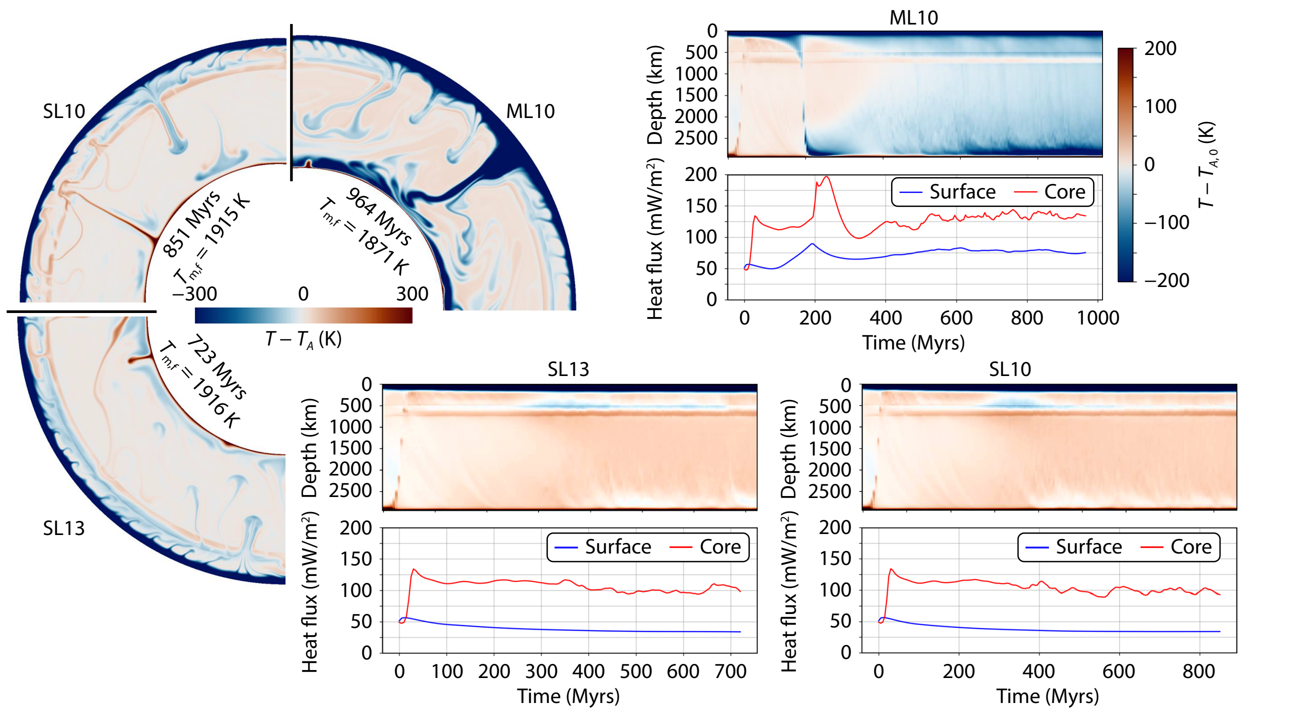

Figure 7. Left: Non-adiabatic temperature field for models SL10, SL13, and ML10, each with initial temperatures of 1900 K and a 30× viscosity increase with depth through the mantle. Right: Depth-averaged temperature deviation from the initial mantle adiabat (top) and the evolution in time of the mean surface and core heat fluxes (bottom) for models SL10, SL13, and ML10.

of hot material from plume conduits, is observed to occur just below the WMF reaction zone. Li RP et al. (2024) provides a schematic diagram how such layering and filtering of plumes might be relevant to different tectonic/volcanic regimes of the early Earth. Additional research into this area is needed, in particular for evaluating the strength and persistence of such laying in the presence of large downwellings.

The mobile lid regime is defined by global recycling of the lithosphere, and thus incorporates the full thickness of the cold thermal boundary layer and the full temperature drop across the surface. Therefore, cold downwellings represent a substantial volume of cold material and are capable of much faster cooling of the interior compared to the stagnant lid regime. In our models, and those of Dannberg et al. (2022), it is the reduced maximum viscosity that permits the entire lithosphere to be recycled. We note that in our 1800–1900 K mantles, the downwellings appear "pinched" in the WMF region before falling into the lower mantle, perhaps as some type of necking instability that is related to this artificially reduced maximum viscosity of cold material. The models of Li RP et al. (2024) were able to achieve recycling of higher viscosity lithosphere by incorporating a plastic rheology which allows yielding of stronger material, however some amount of similar necking appears to be present in those models as well.

Our mobile lid models, as well as those of both Dannberg et al. (2022) and Li RP et al. (2024), observe a partial impedance of mass exchange due to the WMF zone. However, such layering is ephemeral because it is easily overwhelmed by the size and rate of the cold downwellings that drive substantial return flow and disrupt the gradual build-up of material ponding on either side of the MF-dominated edge of the WMF zone. However, in a Venus-like planet with a stagnant lid, the ponding and layering of warm material across the WMF-MF phase change would not be disrupted by such large mass exchanges. The smaller drips forming within a thinner rheological sublayer are much weaker and transport smaller temperature differences and correspondingly smaller viscosity contrasts across the base of the stagnant lid and the ambient mantle. In our models with a hotter mantle (1900 K), there is a clear regime shift between downwellings in the mobile lid compared to those in the stagnant lid, indicating that the convective dynamics in a present-day Venus could be different those of present-day or early Earth that had a mobile lid.

The magnitude of negative thermal expansivity of the WMF phase assemblage, as well as the extent of *P-T* space in which it occurs, are both controlling factors in the propensity of a planet to form mantle avalanches. In our stagnant lid model suite, those with warmer mantle temperatures (>1800 K) allowed increasingly stronger layering to occur within the WMF phase region due to the changing nature of material dripping from the lithosphere (i.e. smaller, more quickly diffused) compared with mobile lid models. The two conditions necessary are: 1) the temperature of the mantle is hot enough that the mantle adiabat intersects with the WMF zone with effective negative thermal expansivity, and 2), the cold deviations of the downwellings from the mantle adiabat remain within the region of phase space where the $wd = mj + fp$ reaction occurs. In other words, the temperature of the cold downwellings must not deviate too greatly from that of the ambient mantle such that they would be denser than the ambient mantle transition zone density in the WMF zone. This condition is better achieved in stagnant lid models, where the temperature drop across the rheological sublayer is a smaller percentage of the temperature drop across the entire lithosphere, compared to that of mobile lid models. Within our suite of stagnant lid models, all of which use a maximum viscosity of 10^{25} Pa·s, only the 1900 K models were hot enough to have both a mantle adiabat and a substantial volume of colder material remaining within the fairly restrictive zone of *P*-*T* space occupied by the WMF assemblage.

The results of these models may be strongly composition dependent. The equation of state used is defined by a HeFESTo look-up table for a bulk pyrolite equilibrium assemblage (18% basalt and 82% harzburgite, from Xu WB et al., 2008). The entropy method in its current formulation in ASPECT is not yet able to handle multiple compositional equations of state as defined by a S-P look-up table, so we assume the mantle is entirely pyrolite material that has not been differentiated by partial melting. Popular paradigms explaining the surface expression of Venus today necessitate a high degree of basalt production in the form of some mechanism of global or regional resurfacing, such as episodic overturn (Armann and Tackley, 2012), to explain the planet's young surface age inferred from the cratering record (Phillips et al., 1992). The compositional consideration is important since harzburgite, the depleted melt product of pyrolite, is predicted to have stable expressions of wadsleyite and ringwoodite along the higher temperature adiabats of 1900 K and would therefore not have a notable WMF reaction zone upon which to layer the cold drips from the lithosphere and generate mantle avalanches. Additionally, recent research has shown that the basalt barrier mechanism at the base of mantle transition zone may trap basaltic crust, were it to subduct or delaminate on Venus (Armann and Tackley, 2012; Vesterholt et al., 2021). This layering mechanism and subsequent break-down could also generate mantle avalanches and large scale surface volcanism on Venus (Papuc and Davies, 2012; Ogawa and Yanagisawa, 2014; Vesterholt et al., 2021; Tian JC et al., 2023). However, we have no present knowledge of the planet's thermal and magmatic evolution before ~500 Myrs ago, nor of the true internal composition. Further research using the entropy formulation to model mantle phase transitions with multiple components will need to be conducted on this front.

Mantle avalanches have previously been reported and studied extensively in thermal convection models with the causation of the ephemeral layering and flushing of upper mantle material attributed to the negative Clapeyron slope of the 660 km phase transition of ringwoodite to bridgmanite + ferropericlase (Machetel and Weber, 1991; Weinstein, 1993; Honda et al., 1993; Tackley et al., 1993; Solheim and Peltier, 1994). The early study by Christensen and Yuen (1984) of layered mantle convection reported a "leaky" layered state due to mantle phase transitions which necessitated a Clapeyron slope of at least −6 MPa/K. The value of the 660 Clapeyron slope, as well as its uncertainty, has decreased since the earliest studies; with seismic studies (e.g. Lebedev et al., 2002; Kaneshima et al., 2012), X-ray diffraction experiments (e.g. Katsura et al., 2003; Fei YW et al., 2004; Litasov and Ohtani, 2005; Litasov et al., 2005; Ishii et al., 2011), and thermodynamic calculations (e.g. Akaogi et al., 1989) putting the Clapeyron slope of Earth's 660 km phase transition between −0.5 and −3 MPa/K (Yanagisawa et al., 2010; Arredondo and Billen, 2016). Generally speaking, numerical models which incorporate mineral physics suggest that as the Clapeyron slope of the 660 transition becomes increasingly negative, the mantle becomes increasingly more layered. Other contributing factors such as viscosity stratification in the upper mantle can aid this layering (Yanagisawa et al., 2010; Rudolph et al., 2015).

The flattening and deflection of subducting slabs is considered contemporary evidence for some degree of layering between the upper and lower mantles at the 660; however, recent studies indicate that the negative Clapeyron slope alone may not account for such behavior. Instead the differing morphology of subducting slabs as seen from tomography could depend on a combination of the 660 endothermic transformation, the buoyancy effects of the slow diffusion rate of the transformation of pyroxene to Majorite (King et al., 2015), upper mantle viscosity structure, trench retreat rate, and slab dip angle (Torii and Yoshioka, 2007; Goes et al., 2017). In our models, we rule out the effects of viscosity stratification as the cause of the layering and mantle avalanches by comparing models SL13 and SL14 with SL10 and SL11, between which there was no notable dynamical difference. We determine it is the zone of reversed buoyancy causing the layering and avalanches and not a result of a radial increase in the depth-dependent reference viscosity due to sharp changes in the adiabatic temperature at the phase transition. Our analysis documents the dynamics of cold drips from the stagnant lid by estimating the buoyancy field which shows a clear positive buoyancy signal for cold accumulating drips. This analysis suggest it is the negative expansivity of the WMF phase assemblage that generates layering in the models. To our knowledge, no previous studies attribute mantle avalanches to the high temperature phase transition of WMF to MF, particularly due to the exotic nature of thermal buoyancy in the WMF region.

Direct evidence of mantle avalanches occurring inside Earth remains elusive, but the phenomena could be indirectly observed in several ways. Cold, dense, and voluminous instabilities falling into the lower mantle can change the inertial tensor of that body, causing a mis-alignment between the principle axis of inertia and the rotation axis, driving a reorientation of the planet i.e. true polar wander (Moser et al., 1997; Machetel and Thomassot, 2002). There are some examples which could be attributed to large scale flushing of the upper mantle, such as the late Cretaceous rapid true polar wander event which occurred at a rate of 3–10 degrees/Myrs (Sager and Koppers, 2000), although the existence of this phenomenon is contested (Cottrell et al., 2023). This event, or others like it, could be tied to other phenomenon such as large igneous province eruptions and a shift in the magnetic polarity of the Earth (Sager and Koppers, 2000). A mantle avalanche could generate a strong upwards return flow of warmer material into the upper mantle which could enhance seafloor spreading rates and associated volcanism (Stein and Hofmann, 1994; Machetel and Humler, 2003). Alternatively, it could destabilize plume generation at the CMB by piling sub-critical convecting material into a critical mass, forming a super-plume (Honda et al., 1993). The arrival of an avalanche to the CMB would cause an increase in heat flux locally from the core, and this skewed perturbation in heat flow could have some baring on the duration of strength or direction of Earth's magnetic field, as suggested in Eide and

Torsvik (1996). The suggestion that mantle avalanches could occur on Venus is new and would need to be investigated further. The presence of multiple large igneous provinces (e.g. the Alta, Beta, and Themis Regios) as well as large regions of deformation (tesserae) could be indicative of strong lateral upper mantle flow associated with the sinking and regional material entrainment into a mantle avalanche.

5. Conclusion

The effective thermodynamic properties of the WMF mineral phase assemblage and the reaction therein can generate sufficient upper mantle layering to produce mantle avalanches in a stagnant lid Venus with mantle temperatures of 1900 K. The presence or absence of mantle avalanches at different mantle temperatures and within the stagnant-lid regime is robust to sizable changes in the viscosity variation with depth and the existence or absence of strong (~10×) viscosity variations locally in the mantle transition zone. Mobile lithosphere in the 1900 K models tends to disrupt transition zone layering before avalanches form, but some avalanches can form in these mantles as well.

The possibility of mantle avalanches occurring in Venus' interior represents a fundamental shift from the expected behavior of mantle convection under stagnant lid (or sluggish lid) conditions. Avalanches driven by intermittent flushing of cold material ponded within the mantle transition zone, due to a zone of reversed buoyancy from the gradual $wd = mj + fp$ transition, allow for larger, more sudden episodes of mass transfer and large scale stirring of the mantle compared to stagnant lid convection in the absence of the WMF phase transition. Mantle avalanches could be occurring inside Venus today, or could have played a role earlier in Venus' history when the mantle temperature was warmer than today.

Acknowledgements

The authors thank J. Dannberg and L. Stixrude for helpful discussions and B. Steinberger and P. Tackley for detailed and thoughtful reviews. The authors are thankful for support from NASA Award 80NSSC22K0100 and U.S. Department of Energy Computational Science Graduate Fellowship under Award Number DE-SC0022158. Computational resources were provided by Extreme Science and Engineering Discovery Environment (XSEDE), which is supported by National Science Foundation grant number ACI-1053575. This research used resources of the National Energy Research Scientific Computing Center (NERSC), a Department of Energy Office of Science User Facility using NERSC award ASCR-ERCAP0026889.

References

Adams, A. C., Stegman, D. R., Smrekar, S. E., and Tackley, P. J. (2022). Regional-scale lithospheric recycling on Venus via peel-back delamination. *J. Geophys. Res.: Planets*, *127*(10), e2022JE007460. https://doi.org/10.1029/2022JE007460

Adams, A. C., Stegman, D. R., Mohammadzadeh, H., Smrekar, S. E., and Tackley, P. J. (2023). Plume-induced delamination initiated at rift zones on Venus. *J. Geophys. Res.: Planets*, *128*(10), e2023JE007879. https://doi.org/10.1029/2023JE007879

Akaogi, M., Ito, E., and Navrotsky, A. (1989). Olivine-modified spinel-spinel transitions in the system Mg_2SiO_4-Fe_2SiO_4: Calorimetric measurements, thermochemical calculation, and geophysical application. *J. Geophys. Res.: Solid Earth*, *94*(B11), 15671–15685. https://doi.org/10.1029/JB094iB11p15671

Armann, M., and Tackley, P. J. (2012). Simulating the thermochemical magmatic and tectonic evolution of Venus's mantle and lithosphere: Two-dimensional models. *J. Geophys. Res.: Planets*, *117*(E12), E12003. https://doi.org/10.1029/2012JE004231

Arredondo, K. M., and Billen, M. I. (2016). The effects of phase transitions and compositional layering in two-dimensional kinematic models of subduction. *J. Geodyn.*, *100*, 159–174. https://doi.org/10.1016/j.jog.2016.05.009

Ballmer, M. D., Schmerr, N. C., Nakagawa, T., and Ritsema, J. (2015). Compositional mantle layering revealed by slab stagnation at ~1000-km depth. *Sci. Adv.*, *1*(11), e1500815. https://doi.org/10.1126/sciadv.1500815

Benešová, N., and Čížková, H. (2012). Geoid and topography of Venus in various thermal convection models. *Stud. Geophys. Geod.*, *56*(2), 621–639. https://doi.org/10.1007/s11200-011-0251-7

Christensen, U. R., and Yuen, D. A. (1984). The interaction of a subducting lithospheric slab with a chemical or phase boundary. *J. Geophys. Res.: Solid Earth*, *89*(B6), 4389–4402. https://doi.org/10.1029/JB089iB06p04389

Christensen, U. R. (1996). The influence of trench migration on slab penetration into the lower mantle. *Earth Planet. Sci. Lett.*, *140*(1-4), 27–39. https://doi.org/10.1016/0012-821X(96)00023-4

Čížková, H., van Hunen, J., van den Berg, A. P., and Vlaar, N. J. (2002). The influence of rheological weakening and yield stress on the interaction of slabs with the 670 km discontinuity. *Earth Planet. Sci. Lett.*, *199*(3-4), 447–457. https://doi.org/10.1016/S0012-821X(02)00586-1

Cottrell, R. D., Bono, R. K., Channell, J. E. T., Bunge, H. P., and Tarduno, J. A. (2023). No Late Cretaceous true polar wander oscillation and implications for stability of Earth relative to the rotation axis. *Earth Planet. Sci. Lett.*, *620*, 118338. https://doi.org/10.1016/j.epsl.2023.118338

Dannberg, J., Gassmöller, R., Li, R. P., Lithgow-Bertelloni, C., and Stixrude, L. (2022). An entropy method for geodynamic modelling of phase transitions: capturing sharp and broad transitions in a multiphase assemblage. *Geophys. J. Int.*, *231*(3), 1833–1849. https://doi.org/10.1093/gji/ggac293

Davaille, A., Smrekar, S. E., and Tomlinson, S. (2017). Experimental and observational evidence for plume-induced subduction on Venus. *Nat. Geosci.*, *10*(5), 349–355. https://doi.org/10.1038/ngeo2928

Eide, E. A., and Torsvik, T. H. (1996). Paleozoic supercontinental assembly, mantle flushing, and genesis of the Kiaman Superchron. *Earth Planet. Sci. Lett.*, *144*(3-4), 389–402. https://doi.org/10.1016/S0012-821X(96)00176-8

Faccenda, M., and Dal Zilio, L. (2017). The role of solid–solid phase transitions in mantle convection. *Lithos, 268–271*, 198–224. https://doi.org/10.1016/j.lithos.2016.11.007

Fei, Y. W., Li, J., Hirose, K., Minarik, W., Van Orman, J., Sanloup, C., van Westrenen, W., Komabayashi, T., and Funakoshi, K. I. (2004). A critical evaluation of pressure scales at high temperatures by in situ x-ray diffraction measurements. *Phys. Earth Planet. Inter., 143–144*, 515–526. https://doi.org/10.1016/j.pepi.2003.09.018

Fleury, A., Plesa, A. C., Hüttig, C., and Breuer, D. (2024). Assessing the accuracy of 2-D planetary evolution models against the 3-D sphere. *Geochem., Geophys., Geosyst.*, *25*(2), e2023GC011114. https://doi.org/10.1029/2023GC011114

Fukao, Y., and Obayashi, M. (2013). Subducted slabs stagnant above, penetrating through, and trapped below the 660 km discontinuity. *J. Geophys. Res.: Solid Earth*, *118*(11), 5920–5938. https://doi.org/10.1002/2013JB010466

Gassmöller, R., Dannberg, J., Bangerth, W., Heister, T., and Myhill, R. (2020). On formulations of compressible mantle convection. *Geophys. J. Int.*, *221*(2), 1264–1280. https://doi.org/10.1093/gji/ggaa078

Glerum, A., Heister, T., Myhill, R., Gassmöller, R., Naliboff, J., Fraters, M., Dannberg, J., and Bangerth, W. (2022). ASPECT v2. 4.0., Zenodo. https://doi.org/10.5281/zenodo.6903424

Goes, S., Agrusta, R., van Hunen, J., and Garel, F. (2017). Subduction-transition zone interaction: A review. *Geosphere*, *13*(3), 644–664. https://doi.org/10.1130/GES01476.1

Hernlund, J. W., and Tackley, P. J. (2008). Modeling mantle convection in the spherical annulus. *Phys. Earth Planet. Inter.*, *171*(1-4), 48–54. https://doi.org/10.1016/j.pepi.2008.07.037

Hirose, K. (2002). Phase transitions in pyrolitic mantle around 670-km depth: Implications for upwelling of plumes from the lower mantle. *J. Geophys. Res.: Solid Earth*, *107*(B4), 2078. https://doi.org/10.1029/2001JB000597

Honda, S., Yuen, D. A., Balachandar, S., and Reuteler, D. (1993). Three-dimensional instabilities of mantle convection with multiple phase transitions. *Science*, *259*(5099), 1308–1311. https://doi.org/10.1126/science.259.5099.1308

Huang, J. S., Yang, A., and Zhong, S. J. (2013). Constraints of the topography, gravity and volcanism on Venusian mantle dynamics and generation of plate tectonics. *Earth Planet. Sci. Lett.*, *362*, 207–214. https://doi.org/10.1016/j.epsl.2012.11.051

Ichikawa, H., Kameyama, M., Senshu, H., Kawai, K., and Maruyama, S. (2014). Influence of majorite on hot plumes. *Geophys. Res. Lett.*, *41*(21), 7501–7507. https://doi.org/10.1002/2014GL061477

Irifune, T., Nishiyama, N., Kuroda, K., Inoue, T., Isshiki, M., Utsumi, W., Funakoshi, K. I., Urakawa, S., Uchida, T., … Ohtaka, O. (1998). The postspinel phase boundary in Mg_2SiO_4 determined by in situ x-ray diffraction. *Science*, *279*(5357), 1698–1700. https://doi.org/10.1126/science.279.5357.1698

Ishii, T., Kojitani, H., and Akaogi, M. (2011). Post-spinel transitions in pyrolite and Mg_2SiO_4 and akimotoite– perovskite transition in $MgSiO_3$: Precise comparison by high-pressure high-temperature experiments with multi-sample cell technique. *Earth Planet. Sci. Lett.*, *309*(3-4), 185–197. https://doi.org/10.1016/j.epsl.2011.06.023

Ishii, T., Kojitani, H., and Akaogi, M. (2018). Phase relations and mineral chemistry in pyrolitic mantle at 1600-2200 °C under pressures up to the uppermost lower mantle: Phase transitions around the 660-km discontinuity and dynamics of upwelling hot plumes. *Phys. Earth Planet. Inter.*, *274*, 127–137. https://doi.org/10.1016/j.pepi.2017.10.005

Ishii, T., Kojitani, H., and Akaogi, M. (2019). Phase relations of harzburgite and MORB up to the uppermost lower mantle conditions: Precise comparison with pyrolite by multisample cell high-pressure experiments with implication to dynamics of subducted slabs. *J. Geophys. Res.: Solid Earth*, *124*(4), 3491–3507. https://doi.org/10.1029/2018JB016749

Ito, E., and Takahashi, E. (1989). Postspinel transformations in the system Mg_2SiO_4-Fe_2SiO_4 and some geophysical implications. *J. Geophys. Res.: Solid Earth*, *94*(B8), 10637–10646. https://doi.org/10.1029/JB094iB08p10637

Jellinek, A. M., Lenardic, A., and Manga, M. (2002). The influence of interior mantle temperature on the structure of plumes: Heads for Venus, Tails for the Earth. *Geophys. Res. Lett.*, *29*(11), 1532. https://doi.org/10.1029/2001GL014624

Kaneshima, S., Kubo, T., and Yoshioka, S. (2012). Geophysical and mineralogical constraints on the post-spinel transformation for the Tonga slab. *Phys. Earth Planet. Inter., 196–197*, 23–31. https://doi.org/10.1016/j.pepi.2012.02.009

Karato, S. I., and Wu, P. (1993). Rheology of the upper mantle: A synthesis. *Science*, *260*(5109), 771–778. https://doi.org/10.1126/science.260.5109.771

Katsura, T., Yamada, H., Shinmei, T., Kubo, A., Ono, S., Kanzaki, M., Yoneda, A., Walter, M. J., Ito, E., … Utsumi, W. (2003). Post-spinel transition in Mg_2SiO_4 determined by high *P*–*T* in situ X-ray diffractometry. *Phys. Earth Planet. Inter.*, *136*(1-2), 11–24. https://doi.org/10.1016/S0031-9201(03)00019-0

Kiefer, W. S., and Hager, B. H. (1991). A mantle plume model for the equatorial highlands of Venus. *J. Geophys. Res.: Planets*, *96*(E4), 20947–20966. https://doi.org/10.1029/91JE02221

King, S. D., Frost, D. J., and Rubie, D. C. (2015). Why cold slabs stagnate in the transition zone. *Geology*, *43*(3), 231–234. https://doi.org/10.1130/G36320.1

Lebedev, S., Chevrot, S., and van der Hilst, R. D. (2002). Seismic evidence for olivine phase changes at the 410-and 660-kilometer discontinuities. *Science*, *296*(5571), 1300–1302. https://doi.org/10.1126/science.1069407

Li, R. P., Dannberg, J., Gassmoeller, R., Lithgow-Bertelloni, C., and Stixrude, L. (2024). How phase transitions impact changes in mantle convection style throughout Earth's history: From stalled plumes to surface dynamics. Authorea Preprints.

Litasov, K., Ohtani, E., Sano, A., Suzuki, A., and Funakoshi, K. (2005). In situ X-ray diffraction study of post-spinel transformation in a peridotite mantle: Implication for the 660-km discontinuity. *Earth Planet. Sci. Lett.*, *238*(3-4), 311–328. https://doi.org/10.1016/j.epsl.2005.08.001

Litasov, K. D., and Ohtani, E. (2005). Phase relations in hydrous MORB at 18-28 GPa: Implications for heterogeneity of the lower mantle. *Phys. Earth Planet. Inter.*, *150*(4), 239–263. https://doi.org/10.1016/j.pepi.2004.10.010

Lithgow-Bertelloni, C., and Richards, M. A. (1998). The dynamics of Cenozoic and Mesozoic plate motions. *Rev. Geophys.*, *36*(1), 27–78. https://doi.org/10.1029/97RG02282

Machetel, P., and Weber, P. (1991). Intermittent layered convection in a model mantle with an endothermic phase change at 670 km. *Nature*, *350*(6313), 55–57. https://doi.org/10.1038/350055a0

Machetel, P., and Thomassot, E. (2002). Cretaceous length of day perturbation by mantle avalanche. *Earth Planet. Sci. Lett.*, *202*(2), 379–386. https://doi.org/10.1016/S0012-821X(02)00785-9

Machetel, P., and Humler, E. (2003). High mantle temperature during cretaceous avalanche. *Earth Planet. Sci. Lett.*, *208*(3-4), 125–133. https://doi.org/10.1016/S0012-821X(03)00041-4

McNamara, A. K., and Zhong, S. J. (2004). Thermochemical structures within a spherical mantle: Superplumes or piles?. *J. Geophys. Res.: Solid Earth*, *109*(B7), B07402. https://doi.org/10.1029/2003JB002847

McNamara, A. K., and Zhong, S. J. (2005). Thermochemical structures beneath Africa and the Pacific Ocean. *Nature*, *437*(7062), 1136–1139. https://doi.org/10.1038/nature04066

Moser, J., Yuen, D. A., Larsen, T. B., and Matyska, C. (1997). Dynamical influences of depth-dependent properties on mantle upwellings and temporal variations of the moment of inertia. *Phys. Earth Planet. Inter.*, *102*(3-4), 153–170. https://doi.org/10.1016/S0031-9201(97)00012-5

Ogawa, M., and Yanagisawa, T. (2014). Mantle evolution in Venus due to magmatism and phase transitions: From punctuated layered convection to whole-mantle convection. *J. Geophys. Res.: Planets*, *119*(4), 867–883. https://doi.org/10.1002/2013JE004593

Papuc, A. M., and Davies, G. F. (2012). Transient mantle layering and the episodic behaviour of Venus due to the 'basalt barrier' mechanism. *Icarus*, *217*(2), 499–509. https://doi.org/10.1016/j.icarus.2011.09.024

Phillips, R. J., Raubertas, R. F., Arvidson, R. E., Sarkar, I. C., Herrick, R. R., Izenberg, N., and Grimm, R. E. (1992). Impact craters and Venus resurfacing history. *J. Geophys. Res.: Planets*, *97*(E10), 15923–15948. https://doi.org/10.1029/92JE01696

Reese, C. C., Solomatov, V. S., Baumgardner, J. R., and Yang, W. S. (1999a). Stagnant lid convection in a spherical shell. *Phys. Earth Planet. Inter.*, *116*(1-4), 1–7. https://doi.org/10.1016/S0031-9201(99)00115-6

Reese, C. C., Solomatov, V. S., and Moresi, L. N. (1999b). Non-newtonian stagnant lid convection and magmatic resur facing on Venus. *Icarus*, *139*(1), 67–80. https://doi.org/10.1006/icar.1999.6088

Rolf, T., Steinberger, B., Sruthi, U., and Werner, S. C. (2018). Inferences on the mantle viscosity structure and the post-overturn evolutionary state of Venus. *Icarus*, *313*, 107–123. https://doi.org/10.1016/j.icarus.2018.05.014

Rudolph, M. L., Lekić, V., and Lithgow-Bertelloni, C. (2015). Viscosity jump in Earth's mid-mantle. *Science*, *350*(6266), 1349–1352. https://doi.org/10.1126/science.aad1929

Sager, W. W., and Koppers, A. A. P. (2000). Late cretaceous polar wander of the pacific plate: evidence of a rapid true polar wander event. *Science*, *287*(5452), 455–459. https://doi.org/10.1126/science.287.5452.455

Sandwell, D. T., and Schubert, G. (1992). Evidence for retrograde lithospheric subduction on Venus. *Science*, *257*(5071), 766–770. https://doi.org/10.1126/science.257.5071.766

Schubert, G., and Sandwell, D. T. (1995). A global survey of possible subduction sites on Venus. *Icarus*, *117*(1), 173–196. https://doi.org/10.1006/icar.1995.1150

Smrekar, S. E., Davaille, A., and Sotin, C. (2018). Venus interior structure and dynamics. *Space Sci. Rev.*, *214*(5), 88. https://doi.org/10.1007/s11214-018-0518-1

Solheim, L. P., and Peltier, W. R. (1994). Avalanche effects in phase transition modulated thermal convection: A model of Earth's mantle. *J. Geophys. Res.:*

Solid Earth, *99*(B4), 6997–7018. https://doi.org/10.1029/93JB02168

Solomatov, V. S. (1995). Scaling of temperature- and stress-dependent viscosity convection. *Phys. Fluids*, *7*(2), 266–274. https://doi.org/10.1063/1.868624

Solomatov, V. S., and Moresi, L. N. (1996). Stagnant lid convection on Venus. *J. Geophys. Res.: Planets*, *101*(E2), 4737–4753. https://doi.org/10.1029/95JE03361

Solomatov, V. S., and Moresi, L. N. (1997). Three regimes of mantle convection with non-Newtonian viscosity and stagnant lid convection on the terrestrial planets. *Geophys. Res. Lett.*, *24*(15), 1907–1910. https://doi.org/10.1029/97GL01682

Stein, M., and Hofmann, A. W. (1994). Mantle plumes and episodic crustal growth. *Nature*, *372*(6501), 63–68. https://doi.org/10.1038/372063a0

Steinberger, B., and Calderwood, A. R. (2006). Models of large-scale viscous flow in the Earth's mantle with constraints from mineral physics and surface observations. *Geophys. J. Int.*, *167*(3), 1461–1481. https://doi.org/10.1111/j.1365-246X.2006.03131.x

Steinberger, B., Werner, S. C., and Torsvik, T. H. (2010). Deep versus shallow origin of gravity anomalies, topography and volcanism on Earth, Venus and Mars. *Icarus*, *207*(2), 564–577. https://doi.org/10.1016/j.icarus.2009.12.025

Stixrude, L., and Lithgow-Bertelloni, C. (2005). Thermodynamics of mantle minerals—I. Physical properties. *Geophys. J. Int.*, *162*(2), 610–632. https://doi.org/10.1111/j.1365-246X.2005.02642.x

Stixrude, L., de Koker, N., Sun, N., Mookherjee, M., and Karki, B. B. (2009). Thermodynamics of silicate liquids in the deep Earth. *Earth Planet. Sci. Lett.*, *278*(3-4), 226–232. https://doi.org/10.1016/j.epsl.2008.12.006

Stixrude, L., and Lithgow-Bertelloni, C. (2011). Thermodynamics of mantle minerals-II. Phase equilibria. *Geophys. J. Int.*, *184*(3), 1180–1213. https://doi.org/10.1111/j.1365-246X.2010.04890.x

Stixrude, L., and Lithgow-Bertelloni, C. (2022). Thermal expansivity, heat capacity and bulk modulus of the mantle. *Geophys. J. Int.*, *228*(2), 1119–1149. https://doi.org/10.1093/gji/ggab394

Tackley, P. J., Stevenson, D. J., Glatzmaier, G. A., and Schubert, G. (1993). Effects of an endothermic phase transition at 670 km depth in a spherical model of convection in the Earth's mantle. *Nature*, *361*(6414), 699–704. https://doi.org/10.1038/361699a0

Thiriet, M., Breuer, D., Michaut, C., and Plesa, A. C. (2019). Scaling laws of convection for cooling planets in a stagnant lid regime. *Phys. Earth Planet. Inter.*, *286*, 138–153. https://doi.org/10.1016/j.pepi.2018.11.003

Tian, J. C., Tackley, P. J., and Lourenço, D. L. (2023). The tectonics and volcanism of Venus: New modes facilitated by realistic crustal rheology and intrusive magmatism. *Icarus*, *399*, 115539. https://doi.org/10.1016/j.icarus.2023.115539

Torii, Y., and Yoshioka, S. (2007). Physical conditions producing slab stagnation: Constraints of the Clapeyron slope, mantle viscosity, trench retreat, and dip angles. *Tectonophysics*, *445*(3-4), 200–209. https://doi.org/10.1016/j.tecto.2007.08.003

Uppalapati, S., Rolf, T., Crameri, F., and Werner, S. C. (2020). Dynamics of lithospheric overturns and implications for Venus's surface. *J. Geophys. Res.: Planets*, *125*(11), e2019JE006258. https://doi.org/10.1029/2019JE006258

van der Hilst, R., and Seno, T. (1993). Effects of relative plate motion on the deep structure and penetration depth of slabs below the Izu-Bonin and Mariana island arcs. *Earth Planet. Sci. Lett.*, *120*(3-4), 395–407. https://doi.org/10.1016/0012-821X(93)90253-6

van Keken, P. (2001). Cylindrical scaling for dynamical cooling models of the Earth. *Phys. Earth Planet. Inter.*, *124*(1-2), 119–130. https://doi.org/10.1016/S0031-9201(01)00195-9

Vesterholt, A. L., Petersen, K. D., and Nagel, T. J. (2021). Mantle overturn and thermochemical evolution of a non-plate tectonic mantle. *Earth Planet. Sci. Lett.*, *569*, 117047. https://doi.org/10.1016/j.epsl.2021.117047

Weinstein, S. A. (1993). Catastrophic overturn of the Earth's mantle driven by multiple phase changes and internal heat generation. *Geophys. Res. Lett.*, *20*(2), 101–104. https://doi.org/10.1029/93GL00044

Widemann, T., Smrekar, S. E., Garvin, J. B., Straume-Lindner, A. G., Ocampo, A. C., Schulte, M. D., Voirin, T., Hensley, S., Dyar, M. D., … Desai, N. (2023). Venus evolution through time: Key science questions, selected mission concepts and future investigations. *Space Sci. Rev.*, *219*(7), 56. https://doi.org/10.1007/s11214-023-00992-w

Xu, W. B., Lithgow-Bertelloni, C., Stixrude, L., and Ritsema, J. (2008). The effect of bulk composition and temperature on mantle seismic structure. *Earth Planet. Sci. Lett.*, *275*(1-2), 70–79. https://doi.org/10.1016/j.epsl.2008.08.012

Yanagisawa, T., Yamagishi, Y., Hamano, Y., and Stegman, D. R. (2010). Mechanism for generating stagnant slabs in 3-D spherical mantle convection models at Earth-like conditions. *Phys. Earth Planet. Inter.*, *183*(1-2), 341–352. https://doi.org/10.1016/j.pepi.2010.02.005